Band-center metal-insulator transition in bond-disordered graphene

Naba P. Nayak,[1] Surajit Sarkar,[1,2] Kedar Damle,[3] and Soumya Bera[1]
[1]*Department of Physics, Indian Institute of Technology Bombay, Mumbai 400076, India*
[2]*Department of Physics, Concordia University, Montreal, Quebec, Canada*
[3]*Department of Theoretical Physics, Tata Institute of Fundamental Research, Mumbai 400005, India*

(Received 14 June 2023; revised 18 October 2023; accepted 14 December 2023; published 5 January 2024)

We study the transport properties of a tight-binding model of noninteracting fermions with random hopping on the honeycomb lattice. At the particle-hole-symmetric chemical potential, the absence of diagonal disorder (random on-site potentials) places the system in the well-studied chiral orthogonal universality class of disordered fermion problems, which are known to exhibit both a critical metallic phase and a dimerization-induced localized phase. Here, our focus is the behavior of the two-terminal conductance and the Lyapunov spectrum in quasi-one-dimensional geometry near the dimerization-driven transition from the metallic to the localized phase. For a staggered dimerization pattern on the square and honeycomb lattices, we find that the renormalized localization length ξ/M (M denotes the width of the sample) and the typical conductance display scaling behavior controlled by a crossover length scale that diverges with exponent $\nu \approx 1.05(5)$ as the critical point is approached. However, for the plaquette dimerization pattern, we observe a relatively large exponent $\nu \approx 1.55(5)$, revealing an apparent nonuniversality of the delocalization-localization transition in the BDI symmetry class.

DOI: 10.1103/PhysRevB.109.035109

I. INTRODUCTION

Quenched disorder plays a significant role in determining electronic transport properties, particularly when quantum interference enhances its effects and leads to Anderson localization phenomena [1–3]. Such disorder effects are controlled crucially by the symmetries of the disordered Hamiltonian. For instance, in a two-dimensional (2D) electron gas with potential scattering from random impurities, the sign of the quantum interference correction for the conductivity depends on whether the electronic system has spin-rotation symmetry. As a result of the important role played by such symmetry considerations, our modern understanding of such phenomena relies heavily on a symmetry-based classification of disordered systems [4,5].

Tight-binding models of free fermions with real-valued random hopping amplitudes on the nearest-neighbor links of a bipartite lattice fall in a particularly interesting symmetry class, labeled BDI by Altland and Zirnbauer in their tenfold classification of disordered systems [4]. Due to the absence of on-site potential energy terms and the bipartite structure of hopping amplitudes, the free-fermion spectrum in this class is distinguished by the presence of a particle-hole symmetry which guarantees that each eigenstate at energy $+\epsilon$ has a partner at energy $-\epsilon$. The band-center energy $\epsilon = 0$ is thus special.

Within the field-theoretical approach pioneered by Gade and Wegner [6,7], the bare conductivity at the band center receives no quantum corrections in two dimensions, while the density of states develops a characteristic "Gade-Wegner" singularity $\rho(\epsilon) \sim |\epsilon|^{-1} \exp[-\ln^{1/x}(1/|\epsilon|)]$ (with $x = 2$) for energies $|\epsilon|$ smaller than a characteristic crossover energy scale controlled by this conductivity. The conclusion is that such particle-hole-symmetric systems can have a critical metallic phase whose low-energy properties are characterized by a fixed line within the field-theoretical renormalization group framework.

As is well known from the work of Dyson and others [8–11], the corresponding one-dimensional (1D) system has a stronger "Dyson singularity" $\rho(\epsilon) \sim |\epsilon|^{-1} \ln^{-y}(1/|\epsilon|)$ (with $y = 3$) in the density of states at the band center. Generalizations to multichannel cases and the nature of the zero-energy wave functions in both 1D and 2D cases have also been studied more recently [12–15].

In the one-dimensional case, this singular behavior can be derived from the properties of an infinite-disorder fixed point of a real-space strong-disorder renormalization group approach [16]. In the 2D scenario, it is difficult to obtain conclusive results from a direct numerical implementation of this strong-disorder renormalization group approach. However, it motivates a closely related strong-disorder analysis [17] of the low-energy properties of the critical metallic phase via a connection to optimal defects in a related dimer model. This real-space approach predicts a singularity of the Gade-Wegner form but corrects the associated exponent to $x = 3/2$.

This prediction of a modified Gade-Wegner form for the band-center singularity in two dimensions was also confirmed by subsequent work [18,19] that refined the original field-theoretical analysis of Gade and Wegner. More recent work also studied the effects of vacancy disorder in such 2D systems, finding that vacancies lead to a stronger Dyson form of the singularity (albeit with nonuniversal y) at intermediate energies before the system crosses over at the lowest energies to the modified Gade-Wegner form [20–22].

The real-space approach of Motrunich *et al.* [17] also predicts that such two-dimensional systems can realize, in addition to the critical metallic phase, a localized Griffiths phase with a weaker nonuniversal power-law divergence

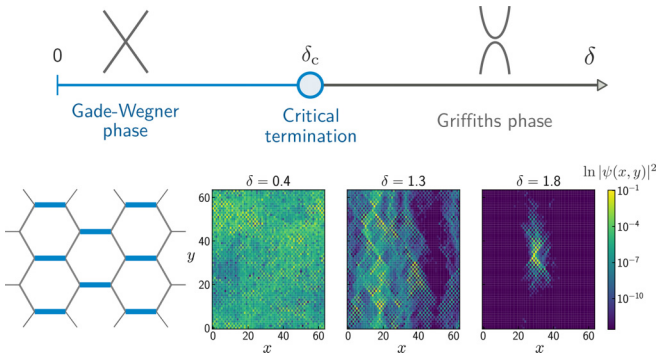

FIG. 1. Top: Schematic phase diagram as a function of dimerization. Without disorder, there is a dimerization-driven transition from semimetal to band insulator. With bond disorder, there is a corresponding transition from a critical metal to a Griffiths insulator [17]. Bottom left: Staggered dimer pattern on a honeycomb flake. Bottom right: $E = 0$ wave function amplitudes $\log|\psi|^2$ for a typical disorder realization of disorder with a staggered dimer pattern (1). The system size is 64×64 with periodic boundary conditions in both directions. The wave function shows more spreading in the critical metal phase compared to the Griffiths phase, as expected.

$\rho(\epsilon) \sim |\epsilon|^{-1+2/z}$ (with nonuniversal z) of the density of states near the band center. As noted in Motrunich *et al.* [17], such a localized phase can be established by strong enough dimerization in the values of the hopping amplitudes (see Fig. 1). While both the critical metallic phase and the localized Griffiths phase have been discussed extensively in the literature, the transition between the two has received much less attention [17,23,24].

Here, we focus on the transport properties of the 2D sample in the vicinity of this transition via numerical studies of both the two-terminal Landauer conductance and the full Lyapunov spectrum λ. The transfer matrix and the Lyapunov spectrum studies provide complementary evidence in favor of or against particular scaling results that are obtained by the renormalization group approach. For small dimerization, the density $\rho(\lambda)$ of Lyapunov exponents λ in quasi-1D geometry is nonzero at $\lambda = 0$. This corresponds [25] to a nonzero conductivity. In this phase, we find that the conductivity extracted from the typical two-terminal conductance is roughly independent of the sample geometry and consistent with the conductivity obtained from the Lyapunov density $\rho(0)$, indicating a metallic phase. With increasing dimerization, the Lyapunov density of states develops a gap around $\lambda = 0$, signaling the transition to a gapped insulating phase at a critical dimerization strength δ_c. A qualitative phase diagram is shown in Fig. 1.

In the gapped insulating phase close to δ_c, we perform a finite-size scaling analysis of the renormalized localization length ξ/M (where $M \gg 1$ is the width of the quasi-1D sample whose length $L \gg M$). For staggered dimerization on both the square and honeycomb lattices, we argue that the rigid shift [17] of the Lyapunov spectrum, characteristic of staggered dimerization, implies that ξ/M diverges as $\sim(\delta - \delta_c)^{-\nu}$, with $\nu = 1$ as δ approaches δ_c from above. The value of ν we obtain from both the Lyapunov spectrum study and direct measurement of the typical two-terminal conductance in the wide-sample geometry is consistent with this prediction within the numerical errors associated with these calculations. A calculation of the transport properties in the direction perpendicular to the strong bonds of the staggered dimerization pattern also yields the same value of ν within numerical uncertainties. However, on the honeycomb lattice, for a more symmetric plaquette dimerization that does not have this rigidity property, we observe a larger exponent $\nu \approx 1.55(5)$. This apparent nonuniversality in the value of the exponent is one of our main findings.

Intriguingly, the larger value of ν that we find for plaquette dimerization on the honeycomb lattice is consistent, within our numerical errors, with a recent prediction [26] of the same exponent in the closely related problem of random bipartite hopping with *complex* hopping amplitudes on the square lattice with the same kind of plaquette dimerization. This falls in Altland-Zirnbauer class AIII, while the systems we study are in class BDI. Since that study also used a plaquette dimerization pattern for the numerical work, it would be interesting in follow-up work to determine whether a similar nonuniversality is also present in the problem with complex hopping amplitudes and explore this apparent nonuniversality within the framework of the theory developed in Ref. [26].

II. MODEL AND OBSERVABLES

We consider a model of free fermions hopping on the honeycomb lattice and an analogous model on the square lattice. In this model, the real-valued nearest-neighbor hopping amplitudes are independent random variables sampled from a uniform distribution. For the conductance calculation, we take a clean one-dimensional lead attached to the disordered sample. The Hamiltonian of the system thus reads

$$\hat{\mathcal{H}} = -\sum_{\langle ij \rangle} t_{ij}(c_i^\dagger c_j + \text{H.c.}), \tag{1}$$

where c_i ($c_i^\dagger$) is the fermion annihilation (creation) operator at site i and the sum is over all nearest-neighbor links $\langle ij \rangle$. We define a dimerization pattern by choosing the hopping strength of selected "dimerized" bonds to be independent random variables uniformly distributed in the range $[0, e^\delta]$, while the hopping amplitudes on other "nondimerized" bonds are random variables drawn uniformly in the range [0,1]. The parameter δ thus represents a dimerization in the mean value of the hopping amplitudes. Since the ratio of the width of the distribution to its mean remains the same, tuning δ changes the dimerization without changing the strength of the bare disorder. In all our numerical simulations, typically, we average over $\sim 10^3$ disorder configurations for the correlation length calculations, and for conductance, typically, we average over $\sim 10^4$ samples unless specified otherwise.

We study both the staggered and plaquette dimerization patterns (described below) on the honeycomb lattice and the staggered pattern on the square lattice to access the dimerization-driven transitions from metallic to localized behavior in this model on both lattices at $E = 0$. The staggered anisotropic pattern was chosen to be a representative of patterns that break the rotational symmetry between the transverse direction and the direction of the

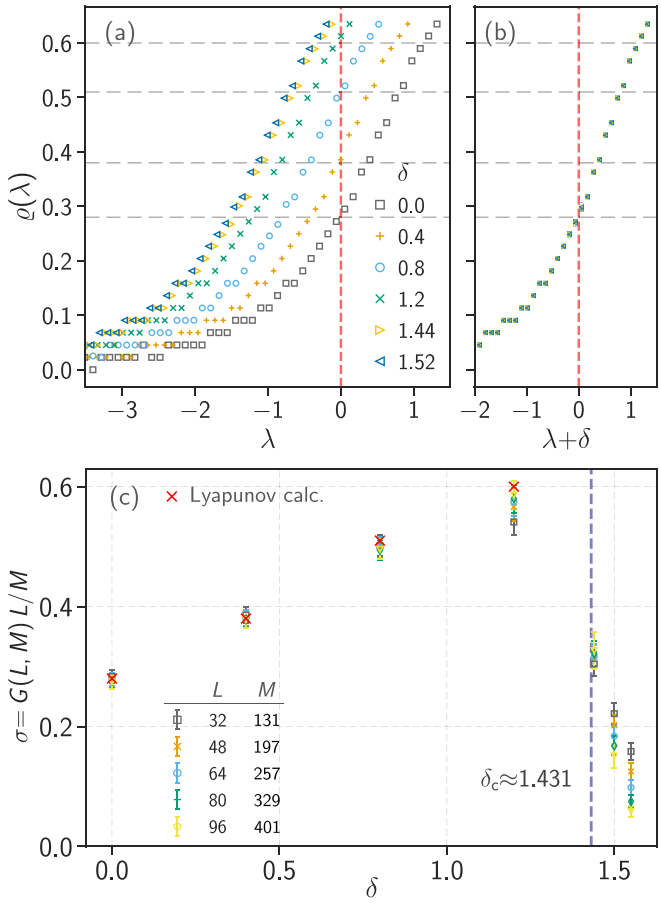

FIG. 2. (a) The Lyapunov spectral density $\rho(\lambda)$ for A-sublattice transfer along the direction of the arrow in the staggered graphene lattice as shown in the inset in Fig. 3(b). With increasing δ, the spectral density shifts rigidly, and the horizontal dotted lines indicate the value where the density curves cut the $\lambda = 0$ axis, i.e., $\rho(\lambda = 0)$, and this gives an estimate of the conductivity (up to a trivial constant) of the sample in the metal phase [25]. (b) The collapse of all curves with the rigid shift by δ. (c) The conductivity $\sigma = G(L, M)L/M$ as a function of δ estimated from the Lyapunov density of states in quasi-1D geometry and the scattering matrix formalism for a wide sample $L/M \sim 1/4$ (see further details in the text). One-dimensional lattice leads are used for the conductance calculation.

current and leads to a rigid shift of the Lyapunov spectrum. The other plaquette pattern was chosen because it maintains the rotational symmetry and does not lead to a rigid shift of the Lyapunov spectrum. Further, note that the staggered dimerization pattern can choose any one out of the three equivalent bond orientations and enhance the corresponding bond strengths. Given the symmetry of the honeycomb lattice, all these choices are equivalent, and the only physical distinction then is in the direction of the current flow relative to the chosen orientation for the staggered pattern.

In the staggered dimerization pattern on the honeycomb lattice [shown in the inset in Fig. 3(b)] the horizontal bonds along the direction of the arrow are dimerized, while along the other direction the bonds are nondimerized in the way defined above. The plaquette dimerization pattern on the honeycomb lattice [shown in the inset of Fig. 5(b)] is a more symmetric pattern that does not single out a particular direction as in the staggered pattern. In this pattern, the strong dimerized bonds are ordered at the three-sublattice wave vector of the underlying triangular Bravais lattice. On the square lattice, we mainly study the staggered pattern, in which the strong dimerized bonds are all of one orientation and arranged in a pattern corresponding to wave vector (π, π). The plaquette dimerization pattern on the square lattice, on the other hand, has strong dimerized bonds that form perimeters of elementary plaquettes that are ordered at wave vectors $(\pi, 0)$ and $(0, \pi)$ and was studied in Ref. [26] with complex hopping amplitudes.

A. Lyapunov analysis

The standard Lyapunov spectrum λ_i of the transfer matrix $T = \prod_n T_n$ (T_n is the transfer matrix for the nth slice) for a quasi-1D geometry of width M is used to study the metal-insulator transition (MIT) [27]. In the quasi-1D limit, the inverse of the smallest Lyapunov exponent in the limit of large L in the localized phase defines the localization length $\xi = 1/\lambda_{\min}$ [25]. The normalized localization length ξ/M [25] is expected to exhibit finite-size scaling across an MIT, allowing one to extract the exponent ν from a finite-size scaling analysis of ξ approaching the transition from the localized side. Moreover, the limiting spectral density of Lyapunov exponents $\{\lambda_i\}$ in such a quasi-1D geometry,

$$\rho(\lambda) = \lim_{M\to\infty} 1/M \sum_i \delta(\lambda - \lambda_i), \tag{2}$$

contains information about the transport properties of the sample (here, the width M of the sample is assumed to increase while maintaining the quasi-1D geometry with $L \gg M$). In particular, the $\lambda = 0$ density of states $\rho(\lambda = 0)$ is finite in a metal and proportional to the conductivity, while it is strictly zero in an insulating phase [25]. Therefore, at a transition to a localized insulating phase, we expect the Lyapunov spectral density to develop a gap in the spectrum at $\lambda = 0$. In our calculation, we use the fact that the Hamiltonian has chiral symmetry. Due to this, the wave functions at $E = 0$ can be chosen to have support only on one sublattice, and the transfer of such a wave function from one side to the other can be performed just on this sublattice; this decoupling allows a trivial factor of two increases in the system width M [17,28] since one can assemble the full Lyapunov spectrum from such a calculation for just one sublattice. The full spectrum $\rho(\lambda)$ is symmetric about $\lambda = 0$, and this symmetry implies that a Lyapunov mode at $+\lambda$ on one sublattice has a partner at $-\lambda$ on the other sublattice, allowing a reconstruction of the full spectrum from this sublattice calculation.

As emphasized earlier [17,28], the staggered dimerization pattern leads to an interesting simplification: The two sublattice Lyapunov spectra at $E = 0$ shift rigidly in opposite directions with increasing δ, all the while maintaining the $\lambda \to -\lambda$ symmetry of the full spectrum (see Appendix A for more details). It is therefore possible to determine the critical value δ_c at which the metal gives way to the insulator simply by knowing the spectrum for one sublattice at $\delta = 0$. For $\delta > \delta_c$ in the insulator, this rigidity also implies that $\lambda_{\min} \sim$

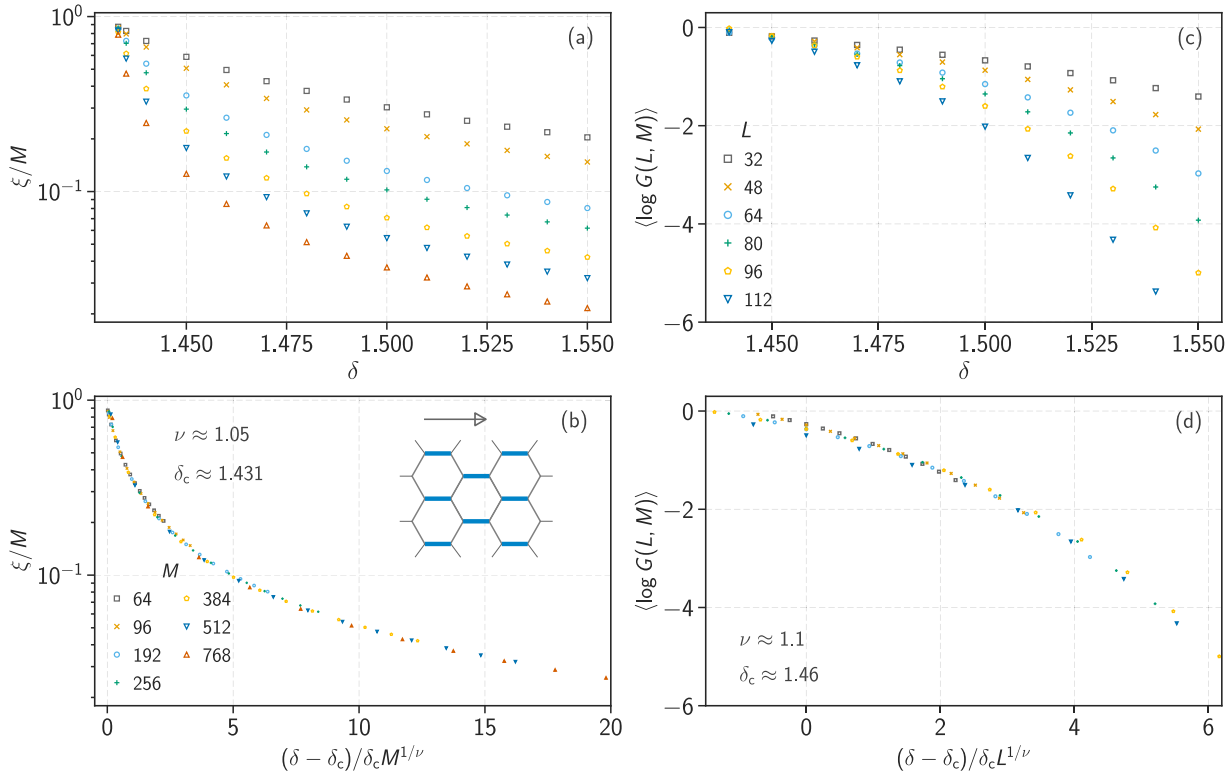

FIG. 3. (a) Results for the staggered dimerization pattern on armchair graphene shown in the inset in (b). The normalized localization length ξ/M for a transfer along the direction of the arrow of the lattice as a function of dimerization δ for different values of width $M = 64$–768 and length $L = 10^5$ in the localized phase. (b) The corresponding finite-size data collapse with critical exponent $\nu \approx 1.05$ and critical dimerization strength $\delta_c \approx 1.431$. (c) $\langle \ln G \rangle$ calculated within the two-terminal setup for the same lattice with 1D clean lattice leads connected along the direction of the arrow in the localized phase for various system lengths $L = 32$–112 for $L/M \sim 1/4$. (d) The corresponding approximate scaling collapse for $\langle \ln G \rangle$, which yields $\nu \approx 1.1$.

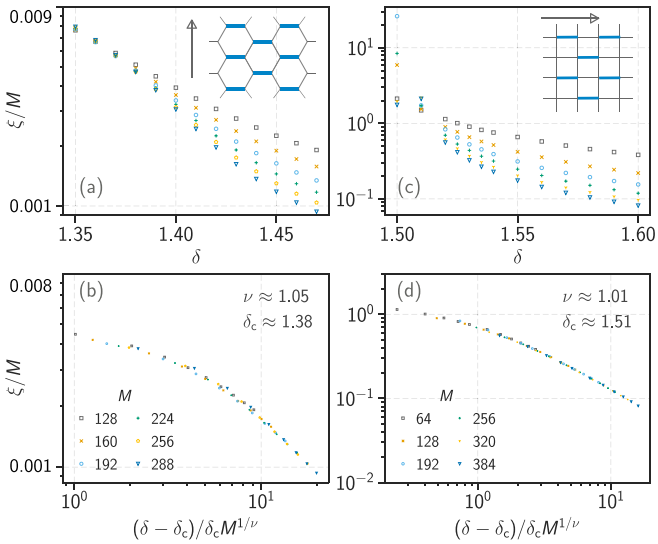

FIG. 4. (a) Renormalized localization length as a function of the dimerization strength δ for the staggered dimerization pattern on the honeycomb lattice in the direction of the arrow shown in the inset. (b) The scaling collapse, which yields $\nu \approx 1.05(5)$. (c) The renormalized localization length ξ/M for the staggered dimerization pattern on a square lattice for transfer along the direction of the arrow. Details are similar to (a). (d) The corresponding data collapse, yielding critical exponent $\nu \approx 1.01(3)$.

$(\delta - \delta_c)$, implying that $\xi/M \sim 1/[M(\delta - \delta_c)]$. This argument suggests that the correlation length exponent ν takes on the value $\nu = 1$ for an MIT driven by such a rigid shift in the sublattice Lyapunov spectrum. It is interesting to note that such an argument is also valid for complex hoppings with a staggered dimerization pattern, but we do not study it further here.

Below we explore the validity of this argument and check if it also controls the scaling of the two-terminal conductance calculated from the scattering wave functions (described below). We also ask if a generic transition, not driven by dimerization patterns that involve a rigid shift, has a different value of ν characterizing its critical behavior.

B. Two-terminal conductance

The two-terminal linear conductance at zero temperature is calculated using the Landauer formula

$$G = \frac{e^2}{h} \sum_{nm} |S_{nm}|^2,$$

where G is the dimensionless conductance (in units of e^2/h) and S_{nm} is the scattering matrix element between scattering channels n and m obtained in terms of the zero-energy wave functions. It relates electrical conductance to the total transmission probability of electron waves through a region of random scatters. As is well known, a closely related analysis

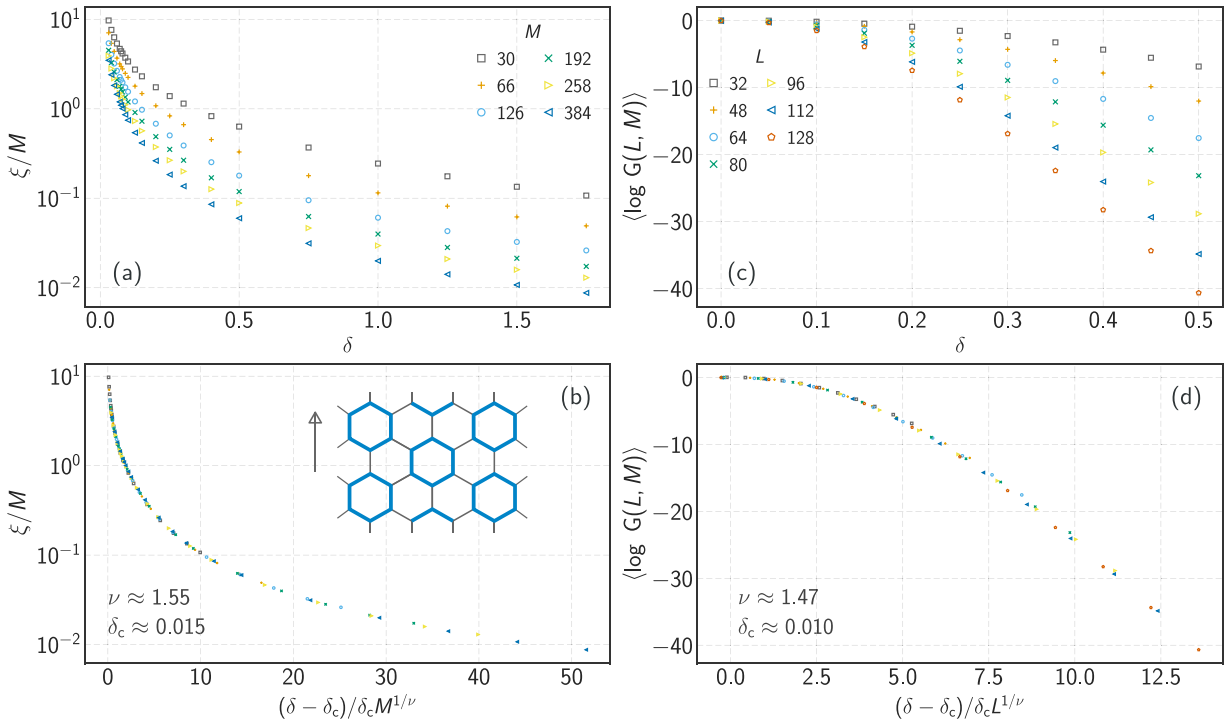

FIG. 5. (a) Results for the plaquette dimerization pattern on armchair graphene as shown in the inset in (b). The normalized localization length ξ/M as a function of dimerization δ for different values of width $M = 30$–384 and length $L = 10^5$ in the localized phase. (b) The corresponding finite-size data collapse with critical exponent $\nu \approx 1.55$ and critical dimerization strength $\delta_c \approx 0.015$. (c) $\langle \ln G \rangle$ calculated within the two-terminal setups for the same lattice with 1D leads connected along the direction of the arrow in the localized phase for various system lengths $L = 32$–128 for $L/M \sim 1/4$. (d) The corresponding approximate scaling collapse for $\langle \ln G \rangle$, which yields $\nu \approx 1.47$.

[29] in terms of Green's functions also leads to the Landauer formula, which relates electrical conductance to the total transmission probability of electron waves through a region of random scatters; in this sense, our results are expected to be equivalent to those obtained from explicit use of the two-terminal Landauer formula.

We used the open-source KWANT package [30], a wave function based method for the conductivity calculation. The "effective" disorder in the system is large, and thus, the conductivity is small, $O(1)$. To avoid small numbers we use a wide geometry $M > L$, which has more conducting channels and ensures a larger value of the conductance. This is useful because the divergent density of states at zero energy gives rise to numerical instability in the opposite limit of a quasi-1D sample. In all our conductance calculations we use one-dimensional lattice leads which allow having a finite density of states in the lead at $E = 0$. The sample width M is chosen in such a way that the clean band structure with armchair edges has linear energy dispersion.

In a generic Anderson delocalization-localization transition, the typical conductance $\exp(\langle \ln G \rangle)$ acts as an order parameter and displays scaling behavior [31]. With this in mind, we study the L and δ dependence of $\langle \ln G \rangle$, and also we monitor the probability distribution of $\ln G$ for a range of L and δ in the metallic phase. We obtain data for the staggered dimerization patterns on both the square and honeycomb lattices and honeycomb lattice data for the plaquette dimerization pattern (Figs. 3 and 4 and their insets).

III. NUMERICAL RESULTS

A. Staggered dimerization on the honeycomb lattice

Lyapunov spectrum and δ_c. The Lyapunov spectral density (2) for the A sublattice transfer along the direction of the arrow in the staggered quasi-1D sample [shown in the inset in Fig. 3(b)] of width $M = 768$ is shown in Fig. 2(a). The curves show a finite density at $\lambda = 0$ in the metallic phase.

Increasing δ further creates a finite gap around the center, i.e., zero spectral density at $\lambda = 0$. This marks the onset of the localized phase of the system, and that allows precise determination of δ_c. The estimated critical disorder strength is found to be $\delta_c \approx 1.431$. In this case, the spectrum does shift rigidly, consistent with the general argument made earlier.

In the Griffiths insulator phase, we see that ξ/M decreases with increasing $\delta - \delta_c$ and M, showing increasing localization, as seen in Fig. 3(a). A one-parameter scaling of ξ/M is performed with the following scaling form: $\xi/M = \mathcal{F}(\chi(w)M^{1/\nu}, \phi(w)M^{y})$ (see Appendix B for more details), where y is the irrelevant scaling exponent. The corresponding data collapse is shown in Fig. 3(b). The estimated critical disorder strength from the analysis is $\delta_c = 1.431(2)$, which is consistent with the critical dimerization value extracted from the Lyapunov density of states (see Fig. 2). The localization length exponent is found to be $\nu = 1.05(5)$, consistent with the theoretical prediction of $\nu = 1$ for cases when the dimerization leads to a rigid shift in the sublattice Lyapunov spectrum.

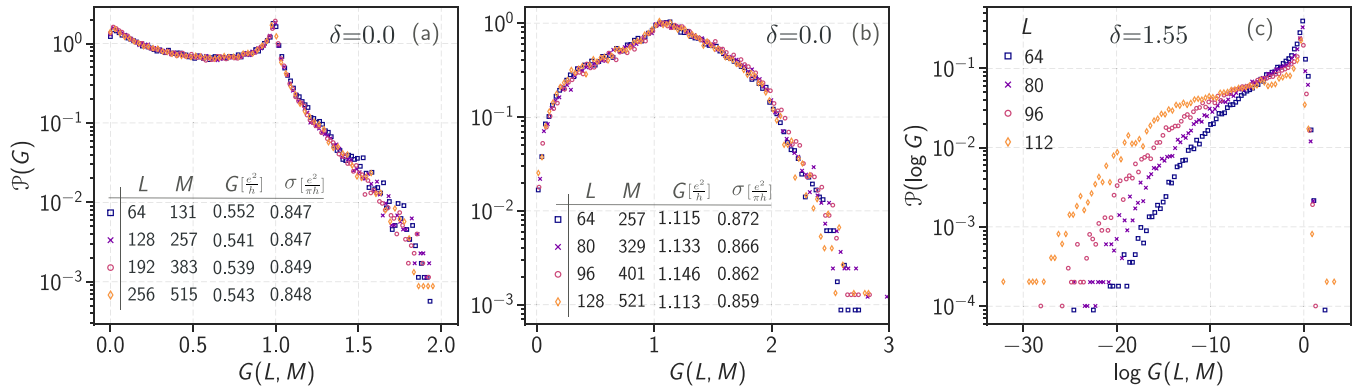

FIG. 6. (a) and (b) Conductance distribution $\mathcal{P}(G)$ at $\delta = 0$ calculated within the two-terminal geometry for the finite staggered honeycomb sample shown in the inset in Fig. 3(b), with two different aspect ratios, $L/M \sim 1/2, 1/4$. The corresponding L and M and the average conductance $G[e^2/h]$ along with the mean conductivity $\sigma[e^2/(\pi h)] \approx 0.85(2)$ are indicated in the legend. (c) The $\ln G$ distribution in the localized phase $\delta = 1.55$ for different sample lengths $L = 64$–112. The open armchair boundary is used for these calculations.

Conductance calculation in localized phase. We compute $\langle \ln G \rangle$ via the scattering matrix formulation as described earlier. In the localized phase, this provides an independent window to these localization properties.

We find that the conductance is exponentially small for $\delta > \delta_c$, i.e., $G \ll 1$, and decreases with system length $L \gg \xi$ as well as with increasing dimerization δ, as shown in Fig. 3(c). We investigate the dependence on δ and M via a finite-size scaling analysis at fixed L/M for wide samples, as shown in Fig. 3(d). The scaling collapse gives a critical disorder of $\delta_c = 1.46(2)$ and exponent $\nu = 1.10(4)$. The marginally higher critical parameters can be attributed to the slightly different geometry, $L/M \approx 1/4$, used for the numerical simulation. Within the available computational resources, we could not directly probe the true 2D limit $L/M = 1$ because that would require simulation of large sample sizes. The estimate of ν obtained in this way is also very close to the value obtained from the Lyapunov exponent analysis; indeed, the theoretical prediction of $\nu = 1$ is just outside the error bars of this numerical estimate.

Additional confirmation of scaling behavior for staggered dimerization. To explore this further, we also determine ν using a Lyapunov spectrum analysis for transfer in the perpendicular direction, i.e., along the zigzag edge of the honeycomb lattice [shown in the inset in Fig. 4(a)]. The results are shown in Fig. 4(a). A one-parameter scaling collapse gives a localization length exponent of $\nu \approx 1.05$, in agreement with the transfer along the other direction. The critical disorder strength is estimated to be $\delta_c \approx 1.38$. The smaller critical disorder strength in this direction could be related to the strong anisotropy of the bond arrangement. We also observe (data not shown) an extremely slow flow towards the larger $\delta_c \sim 1.43$ with increasing system sizes M.

Additionally, we also verify our results for staggered dimer patterns on a square lattice. The main difference here is that the density of states at $E = 0$ is finite in the clean limit compared to the Dirac density of states. The results for the transfer matrix are shown in Fig. 4. A finite-size analysis again predicts the exponent is $\nu \approx 1.01$, in agreement with all our previous estimates of staggered dimer patterns on the honeycomb lattice. Again, we attribute this value of ν to the fact that the Lyapunov spectrum on each sublattice shifts rigidly with δ for this kind of staggered dimerization.

Critical metal phase. Following Chalker and Bernhardt [25] we estimate the average conductivity in the critical metal phase $\sigma = G(L, M)L/M = b\rho(0)$, where b is an order one number and $\rho(0)$ is the Lyapunov density, which is shown in Fig. 2. The two-terminal conductance calculated in the wide sample limit $L/M \ll 1$ is also shown in Fig. 2 as a function of dimerization δ and compares well to the estimate obtained above from the Lyapunov spectrum. In the metallic phase, it increases with δ until the metal-insulator transition point is reached, perhaps reflecting the fact that the strengthened dimerization facilitates transport in the measured direction.

B. Plaquette dimer configuration

The plaquette dimerization pattern on the honeycomb lattice is shown in the inset of Fig. 5(b). This pattern does not single out a particular direction of the lattice as in the case of a staggered pattern. The plaquette dimerization also drives a dimerization-driven critical metal-insulator transition, but with a larger localization length exponent, which could point towards a different fixed point.

The normalized localization length ξ/M and log conductance $\langle \ln G \rangle$ data are shown in Figs. 5(a) and 5(c), respectively. The finite-size analysis of both of our observables [Figs. 5(b) and 5(d)] points towards a higher localization length exponent in this dimer configuration. The localization length predicts the exponent is $\nu \approx 1.55(2)$, which agrees within error bars with the conductance data, which predicts $\nu \approx 1.4(1)$. As noted earlier, recent work in the other chiral class, AIII, indeed predicted a larger exponent $\nu \approx 1.55(1)$ with a similar dimer pattern on the square lattice with complex hopping [26].

C. Conductance distribution

In Fig. 6 we show the distribution of the conductance $G(L, M)$ for the honeycomb lattice in the metallic phase at $\delta = 0$. The data are shown for two different aspect ratios, $L/M = 1/2, 1/4$, in Figs. 6(a) and 6(b). For both aspect ratios the width of $\mathcal{P}(G)$ is independent of the sample L, indicating its scale-invariant properties. While the average conductance, of course, depends on the sample geometry, the conductivity

$\sigma \approx 0.85$ [in units of $e^2/(\pi h)$] for $\delta = 0$ is independent of the sample geometry, indicating that the value is close to its true 2D limit. The distribution $\mathcal{P}(G)$ has a long tail with a singularity at $G \approx 1$ (in units of e^2/h), which is reminiscent of the critical conductance distribution at a 3D metal-insulator transition [32].

In the localized insulating phase, the mean conductance is small $G(L, M) \ll 1$; therefore, we show the log conductance $\ln G$ distribution in Fig. 6(c) at $\delta = 1.55$, which is quite close to δ_c. Deep in the localized phase, the conductance becomes extremely small and suffers from numerical instability. $\mathcal{P}(\ln G)$ is far from a normal Gaussian form, which one would expect in the localized phase [27]. However, we observe the peak at $G \approx 1$ decreases rapidly with L in this regime and the mean conductance becomes smaller. The scaling analysis of the mean G was already presented in Fig. 3.

IV. DISCUSSION AND OUTLOOK

We present a numerical study of transport properties in a bond-disordered tight-binding model of honeycomb and square lattices. The disordered version of the phase transition is allied with the opening of a band gap in the clean model due to dimerization.

From our results for the critical behavior of the mean log conductance and normalized localization length, we find an apparent nonuniversality of critical exponents in the BDI symmetry class. In our analysis we estimated it to be $\nu \approx 1.05(5)$ for the staggered dimer pattern driven localization transition and estimated the critical exponent to be $\nu \approx 1.55(5)$ for the plaquette dimer configuration. It is important to note that with particle-hole symmetry, the localization transition is actually preceded by the critical metal phase that we have discussed here and not by the weak localized phase that is usually observed in the 2D standard Anderson transition. The critical phase itself is a strongly disordered phase, as signaled by small conductivity $\sigma[e^2/\pi h] \lesssim 1$.

At the critical point, we find that the distribution of the conductance is scale invariant. In the range of sizes accessible to our study, this scale invariance remains approximately valid for a range of δ on the metallic side of the transition.

In the immediate vicinity of the transition on the insulating side, the distribution shows a significant deviation from the critical distribution. However, the expected log-Gaussian distribution of log conductance has yet to develop fully in our calculation.

Recently, similar transport statistics were studied in quasi-1D armchair graphene with bond disorder [33]. In that work, the focus was on understanding the crossover phenomenon of the quasilocalized (chiral) critical point to an exponentially localized regime by two parameters scaling with respect to the energy and the system sizes. On the contrary, we are in the 2D limit, where the shape of the conductance fluctuations remains log Gaussian across the phase transition unlike in the 1D model. In particular, we observe system size independent conductance fluctuations close to the critical point, which is absent in the quasi-1D limit.

In the future, it will be relevant to investigate the effects of temperature and interaction on the chiral-symmetric critical point. Exploring the stability of the phase transition and the interaction effects on the universality of the exponent will be important to investigate. Similarly, it will be important to understand the origin of such nonuniversality in the exponent for different dimerization patterns, possibly using the field-theoretical framework that was developed in Ref. [26], particularly when the symmetry of lattice rotations is broken by the dimerization pattern.

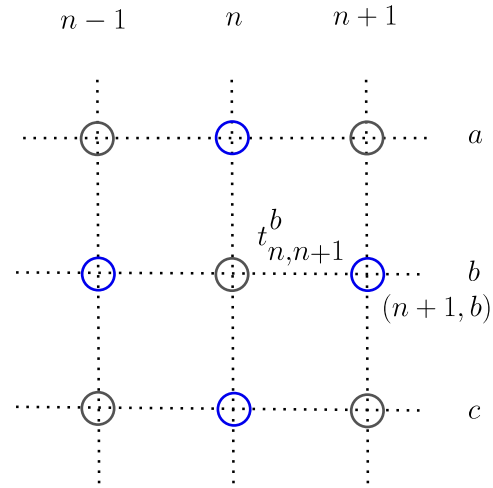

FIG. 7. The 2D square lattice geometry for the transfer matrix calculation. Blue and gray circles represent two different sublattices in this bipartite lattice.

ACKNOWLEDGMENTS

We are grateful to S. Mirlin for pointing out a crucial numerical error in an earlier version of the manuscript and for several discussions. S.B. acknowledges support from SERB-DST, India, through Matrics (Grant No. MTR/2019/000566) and MPG for funding through the Max Planck Partner Group at IITB. N.P.N. acknowledges DST-INSPIRE Fellowship No. IF-190078 for funding. K.D. was supported at the TIFR by DAE, India, and in part by a J. C. Bose Fellowship (JCB/2020/000047) from SERB, DST India, and by the Infosys-Chandrasekharan Random Geometry Center (TIFR).

APPENDIX A: TRANSFER MATRIX AND RIGID SPECTRUM

Here, we discuss the rigid shift in Lyapunov spectrum observed in Fig. 2 in detail. Figure 7 shows part of a 2D square lattice with vertical slices denoted by $(n-1, n, n+1)$, and horizontal slices are denoted by (a, b, c). The hopping $t^b_{n,n+1}$ defines a connection between lattice points (n, b) and $(n+1, b)$.

The wave amplitudes at the slice $n+1$ at $E = 0$ are given by the following transfer matrix [27]:

$$\begin{pmatrix} \psi_{n+1} \\ \psi_n \end{pmatrix} = \begin{pmatrix} \frac{-h_{n,n}}{t_{n,n+1}} & -\frac{t_{n,n-1}}{t_{n,n+1}} \\ \mathbb{1} & 0 \end{pmatrix} \begin{pmatrix} \psi_n \\ \psi_{n-1} \end{pmatrix}, \tag{A1}$$

where $h_{n,n}$ is the Hamiltonian of the nth slice. In a bipartite lattice, the sites can be separated into A sites (blue circles) and B sites (grey circles; see Fig. 7). For the nearest-neighbor Hamil-

TABLE I. Finite-size scaling analysis table for data in Fig. 3(a). N is the number of fitting parameters. The critical parameters (δ_c, ν) are found by fitting the data in Fig. 3(a) to the scaling form in Eq. (B3). The bootstrap error has been obtained by repeated resampling (10000 data points) of the original data and the error is the standard deviation of the resulting sampling distribution. The goodness of fit (GOF) parameter as defined in Eq (B4) is also provided in the table.

L	n_R	n_I	m_R	m_I	N	δ_c	ν	GOF
32–384	6	0	1	0	10	1.430 ± 0.002	1.07 ± 0.04	0.03
32–384	6	0	2	0	11	1.431 ± 0.001	1.05 ± 0.05	0.04
32–384	4	0	1	0	8	1.428 ± 0.005	1.13 ± 0.05	0.16
32–384	4	0	2	0	9	1.431 ± 0.002	1.10 ± 0.06	0.13
32–384	4	1	1	0	11	1.430 ± 0.005	1.04 ± 0.04	0.46
64–384	4	1	1	0	11	1.430 ± 0.003	1.04 ± 0.09	0.51
128–384	4	1	1	0	11	1.431 ± 0.003	1.03 ± 0.05	0.43

tonian defined in Eq. (1), the transfer matrix equation (A1) decouples into individual sublattices at $E = 0$, and the wave function transfer is restricted to one sublattice. The transfer matrix in Eq. (A1) gives the wave amplitude at the lattice site $(n + 1, b)$ as

$$\psi_{n+1,b} = -\frac{t_n^{a,b}}{t_{n,n+1}^b}\psi_{n,a} - \frac{t_n^{b,c}}{t_{n,n+1}^b}\psi_{n,c} - \frac{t_{n-1,n}^b}{t_{n,n+1}^b}\psi_{n-1,b}. \quad \text{(A2)}$$

In particular, for the brick wall (equivalent to honeycomb) lattice the bond $t_{n-1,n}^b = 0$ (see, e.g., Fig. 1), and Eq. (A2) reduces to

$$\psi_{n+1,b} = -\frac{t_n^{a,b}}{t_{n,n+1}^b}\psi_{n,a} - \frac{t_n^{b,c}}{t_{n,n+1}^b}\psi_{n,c}; \quad \text{(A3)}$$

that is, the transfer involves only two slices $(n, n + 1)$ in one iteration. Here, the bonds are distributed equally between [0, 1] with an extra multiplicative factor e^{δ} for the horizontal bonds. Therefore, the multiplicative factor comes out of the transfer matrix multiplication, which is the rigid shift of the spectrum seen in Fig. 2. The magnitude of the shift is proportional to δ, and in this sense the exponent is $\nu = 1.0$ by construction, as explained in the main text.

In contrast, for the square lattice, the wave amplitude $\psi_{n+1,b}$ involves three slices at one iteration of transfer, and the spectrum is nonrigid (not shown here). In this scenario, it is not entirely obvious that $\nu \approx 1$, and therefore, we resort to numerical simulation.

APPENDIX B: FINITE-SIZE SCALING ANALYSIS

This Appendix summarizes the finite-size scaling analysis used to estimate ν and δ_c in the localized phase of the model (Tables I–IV). We follow an approach similar to that in [31,34]

TABLE II. Finite-size scaling analysis table for data in Fig 3(c). Further details are similar to Table-I.

L	n_R	n_I	m_R	m_I	N	δ_c	ν	GOF
32–112	6	0	1	0	10	1.457 ± 0.002	1.11 ± 0.04	0.45
32–112	4	0	1	0	8	1.456 ± 0.002	1.12 ± 0.05	0.46
48–112	4	1	1	0	11	1.455 ± 0.003	1.15 ± 0.09	0.39
64–112	4	1	1	0	11	1.456 ± 0.003	1.13 ± 0.07	0.29

TABLE III. Finite-size scaling analysis table for data in Fig 5(a). Further details are similar to Table-I.

L	n_R	n_I	m_R	m_I	N	δ_c	ν	GOF
30–384	6	0	1	0	10	0.005 ± 0.002	1.64 ± 0.04	0.82
30–384	4	0	1	0	8	0.009 ± 0.003	1.58 ± 0.04	0.26
30–384	4	0	2	0	9	0.005 ± 0.002	1.55 ± 0.05	0.76
66–384	4	1	1	0	11	0.007 ± 0.003	1.54 ± 0.06	0.28
126–384	4	1	1	0	11	0.009 ± 0.003	1.59 ± 0.09	0.43

and expand the scaling function in the leading relevant (χ) and irrelevant (ϕ) scaling variables as follows:

$$\frac{\xi}{M} = \mathcal{F}(\chi(w)M^{1/\nu}, \phi(w)M^{y}), w = (\delta_c - \delta)/\delta_c, \quad \text{(B1)}$$

where $\mathcal{F}$ is a generic scaling function and M is the width of the quasi-1D sample. The irrelevant exponent $y < 0$ characterizes correction to finite-size scaling. The scaling variables are expanded in terms of w as

$$\chi(w) = \sum_{n=0}^{m_R} a_n w^n, \phi(w) = \sum_{n=0}^{m_I} b_n w^n, a_0 = 0. \quad \text{(B2)}$$

A further Taylor expansion of $\mathcal{F}$ leads to

$$\frac{\xi}{M} = \sum_{m}^{n_R}\sum_{n}^{n_I} a_{mn}\chi^m L^{m/\nu}\phi^n L^{ny}\mathbb{F}_{mn}. \quad \text{(B3)}$$

An expansion of Eq. (B3) to order (m_R, m_I, n_R, n_I) gives $N = 2 + m_R + m_I + (n_R + 1)(n_I + 1)$ parameters to fit. An analogous expansion was also used for the observable $\langle \ln G \rangle$ in the main text. We use nonlinear least squares to fit the function to the available data. In the main text, we kept the order of expansion $(m_R, m_I, n_R, n_I) = (1, 0, 4, 0)$ to avoid overfitting of the model. But we checked the stability of the critical exponents to various other orders of expansion (m_R, m_I, n_R, n_I), and the results are summarized in Table IV along with the goodness of fit (GOF), defined as follows:

$$\text{GOF} = \sum_{i=1}^{N_D}(F_i - \Gamma_i)^2/\Gamma_i, \quad \text{(B4)}$$

where F_i is the scaling function evaluated at the ith data point, Γ_i is a numerically observed value at the same data point, and N_D is the number of such data points. The error bars are estimated using the bootstrap resampling of the data set. The irrelevant exponent y is found to be rather large.

TABLE IV. Finite-size scaling analysis table for data in Fig 5(c). Further details are similar to Table-I.

L	n_R	n_I	m_R	m_I	N	δ_c	ν	GOF
32–128	6	0	1	0	10	0.005 ± 0.002	1.47 ± 0.04	0.24
32–128	4	0	1	0	8	0.003 ± 0.002	1.45 ± 0.05	0.56
48–128	6	0	1	0	11	0.015 ± 0.003	1.45 ± 0.09	0.51
64–128	6	0	1	0	11	0.010 ± 0.005	1.44 ± 0.05	0.15
80–128	6	0	1	0	11	0.009 ± 0.003	1.47 ± 0.08	0.18

[1] P. W. Anderson, Absence of diffusion in certain random lattices, Phys. Rev. **109**, 1492 (1958).

[2] P. A. Lee and T. V. Ramakrishnan, Disordered electronic systems, Rev. Mod. Phys. **57**, 287 (1985).

[3] F. Evers and A. D. Mirlin, Anderson transitions, Rev. Mod. Phys. **80**, 1355 (2008).

[4] A. Altland and M. R. Zirnbauer, Nonstandard symmetry classes in mesoscopic normal-superconducting hybrid structures, Phys. Rev. B **55**, 1142 (1997).

[5] C.-K. Chiu, J. C. Y. Teo, A. P. Schnyder, and S. Ryu, Classification of topological quantum matter with symmetries, Rev. Mod. Phys. **88**, 035005 (2016).

[6] R. Gade and F. Wegner, The $n = 0$ replica limit of U(n) and U(n)SO(n) models, Nucl. Phys. B **360**, 213 (1991).

[7] R. Gade, Anderson localization for sublattice models, Nucl. Phys. B **398**, 499 (1993).

[8] F. J. Dyson, The dynamics of a disordered linear chain, Phys. Rev. **92**, 1331 (1953).

[9] G. Theodorou and M. H. Cohen, Extended states in a one-dimensional system with off-diagonal disorder, Phys. Rev. B **13**, 4597 (1976).

[10] T. P. Eggarter and R. Riedinger, Singular behavior of tight-binding chains with off-diagonal disorder, Phys. Rev. B **18**, 569 (1978).

[11] T. A. L. Ziman, Localization and spectral singularities in random chains, Phys. Rev. Lett. **49**, 337 (1982).

[12] P. W. Brouwer, C. Mudry, and A. Furusaki, Density of states in coupled chains with off-diagonal disorder, Phys. Rev. Lett. **84**, 2913 (2000).

[13] M. Titov, P. W. Brouwer, A. Furusaki, and C. Mudry, Fokker-Planck equations and density of states in disordered quantum wires, Phys. Rev. B **63**, 235318 (2001).

[14] G. De Tomasi, S. Roy, and S. Bera, Generalized Dyson model: Nature of the zero mode and its implication in dynamics, Phys. Rev. B **94**, 144202 (2016).

[15] Y. Hatsugai, X.-G. Wen, and M. Kohmoto, Disordered critical wave functions in random-bond models in two dimensions: Random-lattice fermions at $E = 0$ without doubling, Phys. Rev. B **56**, 1061 (1997).

[16] D. S. Fisher, Critical behavior of random transverse-field Ising spin chains, Phys. Rev. B **51**, 6411 (1995).

[17] O. Motrunich, K. Damle, and D. A. Huse, Particle-hole symmetric localization in two dimensions, Phys. Rev. B **65**, 064206 (2002).

[18] C. Mudry, S. Ryu, and A. Furusaki, Density of states for the π-flux state with bipartite real random hopping only: A weak disorder approach, Phys. Rev. B **67**, 064202 (2003).

[19] Y.-Z. Chou and M. S. Foster, Chalker scaling, level repulsion, and conformal invariance in critically delocalized quantum matter: Disordered topological superconductors and artificial graphene, Phys. Rev. B **89**, 165136 (2014).

[20] V. Häfner, J. Schindler, N. Weik, T. Mayer, S. Balakrishnan, R. Narayanan, S. Bera, and F. Evers, Density of states in graphene with vacancies: Midgap power law and frozen multifractality, Phys. Rev. Lett. **113**, 186802 (2014).

[21] P. M. Ostrovsky, I. V. Protopopov, E. J. König, I. V. Gornyi, A. D. Mirlin, and M. A. Skvortsov, Density of states in a two-dimensional chiral metal with vacancies, Phys. Rev. Lett. **113**, 186803 (2014).

[22] S. Sanyal, K. Damle, and O. I. Motrunich, Vacancy-induced low-energy states in undoped graphene, Phys. Rev. Lett. **117**, 116806 (2016).

[23] M. Bocquet and J. T. Chalker, Network models for localization problems belonging to the chiral symmetry classes, Phys. Rev. B **67**, 054204 (2003).

[24] E. J. König, P. M. Ostrovsky, I. V. Protopopov, and A. D. Mirlin, Metal-insulator transition in two-dimensional random fermion systems of chiral symmetry classes, Phys. Rev. B **85**, 195130 (2012).

[25] J. T. Chalker and M. Bernhardt, Scattering theory, transfer matrices, and Anderson localization, Phys. Rev. Lett. **70**, 982 (1993).

[26] J. F. Karcher, I. A. Gruzberg, and A. D. Mirlin, Metal-insulator transition in a two-dimensional system of chiral unitary class, Phys. Rev. B **107**, L020201 (2023).

[27] P. Markoš, Numerical analysis of the Anderson localization, Acta Phys. Slov. **56**, 561 (2006).

[28] O. I. Motrunich, Particle-hole symmetric localization problems in one and two dimensions, Ph.D. thesis, Princeton University, 2007, https://ui.adsabs.harvard.edu/abs/2001PhDT.....200M/abstract.

[29] H. U. Baranger and A. D. Stone, Electrical linear-response theory in an arbitrary magnetic field: A new fermi-surface formation, Phys. Rev. B **40**, 8169 (1989).

[30] C. W. Groth, M. Wimmer, A. R. Akhmerov, and X. Waintal, Kwant: A software package for quantum transport, New J. Phys. **16**, 063065 (2014).

[31] K. Slevin, P. Markoš, and T. Ohtsuki, Reconciling conductance fluctuations and the scaling theory of localization, Phys. Rev. Lett. **86**, 3594 (2001).

[32] P. Markoš, Dimension dependence of the conductance distribution in the nonmetallic regimes, Phys. Rev. B **65**, 104207 (2002).

[33] S. Kasturirangan, A. Kamenev, and F. J. Burnell, Two parameter scaling in the crossover from symmetry class BDI to AI, Phys. Rev. B **105**, 174204 (2022).

[34] K. Slevin and T. Ohtsuki, Corrections to scaling at the Anderson transition, Phys. Rev. Lett. **82**, 382 (1999).